Research Paper

A Turn-On Optoacoustic Probe for Imaging Metformin-Induced Upregulation of Hepatic Hydrogen Sulfide and Subsequent Liver Injury

Lihe Sun, Yinglong Wu, Junjie Chen, Jun Zhong, Fang Zeng✉, Shuizhu Wu✉

State Key Laboratory of Luminescent Materials & Devices, College of Materials Science & Engineering, South China University of Technology, Guangzhou 510640, China.

✉ Corresponding authors: Prof. F. Zeng & Prof. S. Z. Wu, South China University of Technology, 381 Wushan road, Guangzhou 510640, China. Email: shzhwu@scut.edu.cn; mcfzeng@scut.edu.cn; Fax: +86 20 22236262; Tel: +86 20 22236262.

Abstract

Metformin is currently the most prescribed oral agent for diabetes treatment; however the overdose or long-term use may cause some severe side effects such as liver injury. Researches indicate that metformin-induced liver injury is closely related to upregulation of hepatic H_2S. Hence, monitoring hepatic H_2S generation induced by metformin could be an effective approach for evaluating hepatoxicity of the drug.

Methods: We present a novel turn-on and dual-mode probe for detecting and imaging metformin-induced liver injury by specifically tracking the upregulation of hepatic H_2S with fluorescent and optoacoustic methods. After reaction with H_2S, the strong electron-withdrawing group dinitrophenyl ether (which acts as both the recognition moiety and the fluorescence quencher) was cleaved and replaced by an electron-donating group hydroxyl. This correspondingly leads to the changes of the probe's electronic state and absorption red-shifting as well as the subsequent turn-on fluorescent and optoacoustic signals.

Results: The probe was applied to the colon tumor-bearing mice model and the metformin-induced liver injury mice model to achieve tumor imaging and liver injury assessment. The biosafety of the probe was verified by histological analysis (hematoxylin and eosin staining) and serum biochemical assays.

Conclusion: The probe responds quickly to H_2S in tumors and the liver, and MSOT imaging with the probe offers cross-secitonal and 3D spatial information of liver injury. This study may provide an effective approach for accessing medication side effects by tracking drug-metabolism-related products.

Key words: optoacoustic, imaging, metformin, hydrogen sulfide

Introduction

In vivo metabolism of many drugs, especially those require continuous administration over prolonged period of time, has been found to be associated with some adverse side effects, including hepatic injury [1-3]. Some drug-induced liver injury is benign and could be improved after drug discontinuation but a lot more may progress to chronic liver diseases or even acute liver failure [4, 5]. This is probably the reason why drug-induced liver injury has become one of the most challenging disorders for gastroenterologists and usually is the most frequent cause for withdrawing approved drugs. Hence, evaluating liver injury via in-situ detecting the elevation of drug-metabolism-related products at the hepatic region would be helpful in drug development and medication safety improvement.

Metformin is a medicine commonly used in diabetes treatment and has become the most prescribed oral hypoglycemic agent which needs to be taken over a long period of time [6]. It has also been found to be functional in cardiovascular diseases [7-8], cancer [9-11] and other diseases, and it can even help to eliminate nicotine withdrawal syndrome [12]. But long-term use or overdose of metformin can cause some side effects, such as heartburn, stomach pain, and liver or kidney problems [13, 14]. Previous researches indicate that metformin administration may induce hepatotoxicity which is closely related to the drug-induced upregulation of hydrogen sulfide (H_2S) in the hepatic region [15-18]. H_2S is endogenously synthesized during cysteine metabolism primarily in liver and vasculature [19], involved in various physiological and pathological processes [20, 21]. And its toxic effects are dose-related [20, 21]. As the key regulatory site for H_2S, the liver is uniquely predisposed to be subject to high levels of H_2S from endogenous generation and exogenous source. The oxidation of H_2S by liver mitochondria exposes the liver to periods of tissue hypoxia, which contributes to hepatic injury via increased generation of reactive oxygen species [15, 22, 23]. When the metformin-induced H_2S expression is excessive, severe hepatic tissue hypoxia occurs, thus resulting in liver injury. Therefore, monitoring hepatic H_2S generation induced by metformin could be an effective approach for evaluating liver injury/hepatoxicity of the drug.

Compared with other conventional biological detection methods, optical imaging has its advantages of real-time noninvasive imaging and high resolution; for example, fluorescence method has been widely applied in the research of molecular biology and metabolism of small molecules [24-28]; but fluorescence method has unsatisfactory imaging penetration depth due to low spatial resolution with strong light scattering in tissue [29-34]. In contrast, optoacoustic imaging technique avoids the inherent limitations of fluorescent imaging [35-41] and in the meantime retains other superior properties by combining the advantages of both optical imaging and acoustic imaging via detecting the ultrasonic signal generated by local tissue expansion after absorption of the external excitation laser [42-45]. In this situation, the excitation light only needs to enter the biological tissue in one direction instead of traveling back and forth, thereby reducing light scattering and deepening imaging penetration [46-54]. Especially, multispectral optoacoustic tomography (MSOT) [38, 39, 55-57] can distinguish ultrasound signals generated by exogenous contrast agents from the background signals of endogenous substances such as hemoglobin, melanin and so on by irradiating the sample with multiple wavelengths and detecting ultrasound waves and through spectral unmixing and deconvoluting the ultrasound waves emitted by different absorbers. Hence, MSOT allows each photoabsorber to be separately visualized in the target tissue. Furthermore, by volumetric imaging technique or by rendering stacks of 2D images as 3D images, three-dimensional (3D) MSOT images can be generated. Correspondingly, the roles of H_2S in physiological and pathological processes have evoked interest among many researchers; and fluorescent probes for imaging endogenous H_2S have been continuously developed [58-60]. However optoacoustic probes for imaging H_2S are still rare [61] especially that using MSOT imaging [62]. Considering the above and endeavoring toward developing a molecular probe for detecting hepatic H_2S level and subsequent liver injury via optoacoustic imaging, in this study, we synthesized a turn-on probe NR-NO_2 for H_2S detection and imaging. In this probe, a benzothiazole-xanthene dyad serves as the reporting unit, while a dinitrophenyl ether group acts as both the recognition moiety for H_2S and the fluorescence quencher. In the absence of the H_2S, the fluorescence of the probe is quenched due to the existence of the strong electron-withdrawing group dinitrophenyl ether. The presence of H_2S cleaves the strong electron-withdrawing group dinitrophenyl ether and generates an electron-donating group hydroxyl, leading to the changes of the electronic state of the probe molecule and red-shifting of absorption as well as the subsequent turn-on fluorescent and optoacoustic signals. We used the probe (NR-NO_2) to detect liver injury through its specific responding to the elevated level of H_2S in the liver induced by the overdosed metformin in mice model. The schematic illustration for the probe's detection is displayed in Figure 1C, and the experimental results indicate that, the probe responds quickly to H_2S in the liver, and the MSOT imaging with the probe provides cross-sectional and 3D spatial information of liver injury via optoacoustic tomography (OA) imaging.

Material and methods

Preparation of the probe (NR-NO_2)

Synthesis of Compound 1

Dimethylformamide (20 mL, 270 mmol) was added to a 100 mL two-neck round flask under a nitrogen atmosphere. Then, phosphorus oxychloride (20 mL, 130 mmol) dissolved in 20 mL of dichloromethane was slowly added at 0°C. The reaction system was transferred to room temperature, stirred for 30 min, and then cyclohexanone (5 g, 50 mmol) was slowly added. The temperature was raised

to 80 °C and the mixture was refluxed for 2 hours. Afterwards, the resulting mixture was cooled down and poured into ice-cold water and allowed to stand in a refrigerator overnight. The suspension was filtered and precipitate was collected and dried in vacuum as yellow solid (5.0 g, yield: 57%).

Synthesis of Compound 2

Compound 1 (0.34 g, 2 mmol), 3-ethyl-2-methyl-benzothiazolium iodide (1.22 g, 4 mmol) and sodium acetate (0.33 g, 4 mmol) were dissolved in acetic anhydride (20 mL). The mixture was refluxed at 130 °C for 1 h under nitrogen atmosphere. The solvent was removed by vacuum-rotary evaporation procedure, and the resulting green solid mixture was purified by silica gel chromatography with dichloromethane/methanol (20:1) as eluent to obtain Compound 2 as a dark green solid (0.876 g, yield: 89%). ^{1}H NMR (600 MHz, DMSO-d_6, δ ppm): 7.94 (d, J = 7.9 Hz, 2H), 7.71 (d, J = 8.3 Hz, 2H), 7.52 (t, J = 7.8 Hz, 2H), 7.33 (t, J = 7.6 Hz, 2H), 6.46 (d, J = 13.5 Hz, 2H), 6.17 (d, J = 2.2 Hz, 2H), 4.44 (q, J = 7.1 Hz, 4H), 2.66 (t, J = 6.0 Hz, 4H), 1.83 (dd, J = 11.8, 6.0 Hz, 2H), 1.31 (t, J = 7.2 Hz, 6H). ESI-MS (m/z): 490.5 [M]$^+$.

Synthesis of Compound 3 (NR-OH)

Resorcinol (0.44 g, 4 mmol) and potassium carbonate (0.55 g, 4 mmol) were dissolved into 50 mL of dimethylformamide and the mixture was stirred for 10 min. Afterwards, compound 2 (0.8 g, 1.6 mmol) was added into the mixture and the system was stirred at 60 °C for 5 h. The solvent was removed by vacuum-rotary evaporation procedure, and the resulting blue solid mixture was purified by silica gel chromatography with dichloromethane/methanol (20:1) as eluent to obtain Compound 3 as a dark blue solid (0.58 g, yield: 93%). ^{1}H NMR (600 MHz, DMSO-d_6, δ ppm): 9.14 (s, 1H), 8.31 (d, J = 14.6 Hz, 1H), 8.23 (d, J = 7.9 Hz, 1H), 8.07 (d, J = 8.4 Hz, 1H), 7.75 (t, J = 7.4 Hz, 1H), 7.63 (t, J = 7.7 Hz, 1H), 7.34 (d, J = 8.4 Hz, 1H), 6.86 (d, J = 14.6 Hz, 1H), 6.79 (s, 1H), 6.21 – 6.15 (m, 2H), 4.74 (q, J = 7.0 Hz, 2H), 2.69 – 2.61 (m, 4H), 1.85 – 1.77 (m, 2H), 1.40 (t, J = 7.1 Hz, 3H). ESI-MS (m/z): 387.3 [M]$^+$. ^{13}C NMR (151 MHz, d6-DMSO) δ 161.41, 158.91, 158.36, 154.26, 142.59, 141.47, 131.58, 130.14, 129.38, 129.17, 127.52, 127.30, 126.04, 124.26, 115.74, 112.34, 106.64, 102.94, 102.33, 43.44, 28.95, 24.77, 20.54, 13.92.

Synthesis of Compound 4 (NR-NO₂, the probe)

Compound 3 (0.12 g, 0.3 mmol) and potassium carbonate (0.21 g, 1.5 mmol) were dissolved into 10 mL of dimethylformamide and the mixture was stirred for 10 min. Afterwards, 2,4-dinitro-1-fluoro-benzene (75 μL, 0.6 mmol) was added into the mixture

and the system was stirred at 75 °C for 1 h. The solvent was removed by vacuum-rotary evaporation procedure, and the resulting blue solid mixture was purified by silica gel chromatography with dichloromethane/methanol (20:1) as eluent to obtain Compound 4 as a purple solid (0.3 g, yield: 90%). ^{1}H NMR (600 MHz, DMSO-d_6, δ ppm): 8.94 (s, 1H), 8.50 (d, J = 9.3 Hz, 1H), 8.32 (d, J = 14.9 Hz, 1H), 8.21 (d, J = 7.9 Hz, 1H), 8.14 (d, J = 8.5 Hz, 1H), 7.77 (t, J = 7.8 Hz, 1H), 7.66 (t, J = 7.7 Hz, 1H), 7.57 (d, J = 8.5 Hz, 1H), 7.39 (d, J = 5.9 Hz, 2H), 7.22 (s, 1H), 7.14 (d, J = 8.4 Hz, 1H), 7.01 (d, J = 14.9 Hz, 1H), 4.79 (q, J = 7.1 Hz, 2H), 2.72 – 2.63 (m, 4H), 1.84 – 1.77 (m, 2H), 1.39 (t, J = 7.1 Hz, 3H). ESI-MS (m/z): 554.1 [M]$^+$. ^{13}C NMR (151 MHz, d6-DMSO) δ 170.60, 156.15, 155.69, 154.44, 153.65, 142.65, 142.56, 141.46, 140.28, 130.15, 129.65, 129.51, 129.28, 128.31, 128.13, 127.78, 124.29, 123.34, 122.44, 120.89, 120.06, 116.90, 116.34, 113.31, 107.95, 43.99, 29.22, 24.63, 20.35, 14.16.

Optical characterization

Optical spectra were measured using Hitachi U-3010 UV-vis spectrophotometer and Hitachi F-4600 fluorescence spectrophotometer. As for optical spectra measurements, including absorption spectra and fluorescence spectra, in the final test system, the probe concentration was 10 μM, the volume percent of DMSO was 10% and the experimental pH was maintained at 7.4 by PBS. Fluorescence spectra were recorded with excitation at 680 nm. For H₂S response measurement, NaHS was used as the H₂S donor, different concentrations of NaHS were added to the solutions to track the response process for 20 min (spectra were acquired every 2 min). The fluorescence selectivity and limit of detection tests were also performed in the same test conditions. Moreover, we conducted optical response experiments at pH from 6.5 to 7.8.

Phantom optoacoustic imaging

Phantom optoacoustic imaging was conducted with MSOT system (inVision 128, iThera Medical GmbH). The test solutions containing 10 μM NR-NO₂ (or NR-OH) and different concentrations of NaHS were stirred for 20 min at room temperature, then added into NMR sample tube for phantom optoacoustic imaging.

Cell viability assay

The cytotoxicity of the probe was evaluated by MTT assay. Three cell lines (L929, HeLa and HCT-116) were purchased from KeyGEN BioTECH. The cells were cultured in medium (L929 & HeLa: DMEM; HCT-116: McCoy's 5A) added with 10% fetal bovine serum (FBS), 100 U/mL penicillin and 100 μg/mL streptomycin. Culture atmosphere was controlled at

37 °C under 5% CO_2 atmosphere. After a period of culture, the cells were seeded in 96-well plates (about 5000 cells/well) and cultured for 24 h. The medium was washed out with PBS (1X, pH=7.4) and replaced with new medium containing NR-NO$_2$ (concentration: 0, 1, 5, 10, 20, and 50 μM, containing 0.2% DMSO) for one more 24 h. To reduce experimental error, we prepared 8 parallel samples for each concentration. The third day, the medium was washed out and replaced with new medium containing 0.5 mg/mL MTT, then incubated for another 2 h. Finally, the medium in each well was washed out and replaced with 150 μL DMSO to dissolve the precipitates. We used Thermo MK3 ELISA reader to measure the absorbance at 570 nm and estimate the viability of cells in each well.

Flow cytometry

Cell uptake and activation of NR-NO$_2$ was measured by flow cytometry. Three cell lines (L929, HeLa and HCT-116) were seeded into six-well plates at 2×10^5 cells/mL and cultured for 24 h before treatment. The second day, cells were incubated with 30 μM NR-NO$_2$ and cultured for 0, 30 and 90 min respectively. After culturing for the corresponding period of time, the cells were washed, trypsinized, centrifuged and dispersed into a single cell suspension (in PBS). Then, around 10,000 cells were used for analysis on a BD CS6 flow cytometer. The signals in FL3 channel were collected.

Cell imaging

Fluorescence images of living cells were acquired through an Olympus IX71 inverted fluorescence microscope with a DP72 color CCD. Three cell lines (L929, HeLa and HCT-116) were cultured in medium containing different concentrations of NR-NO$_2$ for different lengths of time. Among them, both L929 and HeLa cells were incubated with 30 μM NR-NO$_2$ for 90 min. For HCT-116 cells, the probe concentration and incubation time were performed in these following combinations: 0 μM & 90 min, 10 μM & 90 min, 30 μM & 90 min, 50 μM & 90 min, 30 μM & 0 min, 30 μM & 30 min and 30 μM & 150 min. In addition, aminooxyacetic acid (AOAA) was chosen as an inhibition of cystathionine β synthase (CBS) to reduce the generation of endogenous H$_2$S in HCT-116. HCT-116 cells were incubated with 200 μM AOAA for 30 min, washed by PBS twice, and then incubated with NR-NO$_2$ (30 μM) for 30 min before imaging.

Animal experiments

The BALB/c nude mice (female, 5- 6 weeks old) were provided by Guangdong Medical Laboratory Animal Center (GDMLAC). All animals were allowed to accept standard care (including aseptic environment, autoclaved rodent diet, sterile water and light/dark cycle of 12 h) in Laboratory Animal Center of South China Agricultural University. Mice were randomly assigned to establish different animal models and support subsequent experimental investigations. Groups were randomly divided with 6 mice per group, ensuring sufficient replication of results and a reduction in animal number. In the case of lethal experimental procedures, mice would be euthanized by exposure to carbon dioxide gas. All the experimental protocols were approved by the Ethics Committee of Laboratory Animal Center of South China Agricultural University.

Mice model

The tumor-bearing mice model was established by subcutaneous injection of HCT-116 cells (2×10^6 cells in 100 μL PBS per mouse) at the back of nude mice. Tumors were then allowed to grow for 1-2 weeks before imaging. For the metformin-induced liver injury mice model, the study protocol included: metformin was dissolved in a saline solution, which was then administered via intraperitoneal injection with dosage of 1 mg or 2 mg metformin daily at 10:00 a.m. for 5 consecutive days (each administration of 200 μL). The control group received intraperitoneal injection of physiological saline with the same volume [15].

Animal fluorescence imaging

Animal fluorescence (*in vivo* and *ex vivo*) imaging was performed using Ami small animal imaging system (Spectral Instruments Imaging Co.). For the tumor-bearing mice model, the probe (1.4 mg probe/kg body weight, in PBS containing 4% DMSO) was administered through subcutaneous intratumoral injection. Then, the mice were anesthetized and imaged for 60 min (images were acquired every 10 min) to track the response towards endogenous H$_2$S in tumor. In addition, we also studied the imaging of exogenous H$_2$S in tumor by intratumoral injection of NaHS (1 mM, in PBS, 20 μL). The mice were imaged at 30 min after injection of probe; then NaHS was injected into tumor and imaged again 5 min later. Furthermore, we decreased the level of endogenous H$_2$S in HCT-116 tumors by intratumorally pretreating mice with 100 nmol AOAA for 12 h to inhibit the expression of CBS, and then injected NR-NO$_2$ into tumor at 30 min before *in vivo* fluorescence imaging. For the metformin-induced liver injury mice model, 1 mg metformin-treated mice were intravenously injected with the probe (2.8 mg probe/kg body weight, in PBS containing 2% DMSO) for tracking the probe's metabolism *in vivo*. In addition, we also

studied the imaging of endogenous and exogenous H_2S in the peritoneal cavity of mice by intraperitoneal injection. The groups were healthy mouse with probe injection and healthy mouse with injection of both probe and NaHS (the probe: 2.8 mg probe/kg body weight, in PBS containing 2% DMSO; NaHS: 1 mM, in PBS, 200 µL). In all the experiments mentioned in this paragraph, excitation filter of 675 nm and emission filter of 710 nm were used. All imaging parameters were kept constant for the same mice model.

Animal optoacoustic imaging

Animal optoacoustic imaging was conducted with MSOT system (inVision 128, iThera Medical GmbH). For the tumor-bearing mice model, the probe (1.4 mg probe/kg body weight, in PBS containing 4% DMSO) was administered through subcutaneous intratumoral injection; the mice were anesthetized and placed in the prone position in animal holder for imaging at 30 min post injection of NR-NO$_2$. Furthermore, we decreased the level of endogenous H_2S in HCT-116 tumors by intratumorally pretreating mice with 100 nmol AOAA for 12 h to inhibit the expression of CBS, and then injected NR-NO$_2$ into tumor 30 min prior to *in vivo* optoacoustic imaging. Cross-sectional images were acquired through the whole tumor with a step size of 0.1 mm. For the metformin-induced liver injury mice model, the mice were injected with the probe (2.8 mg probe/kg body weight, in PBS containing 2% DMSO) via tail vein and then imaged for 60 min (images were acquired every 15 min). Mice were anesthetized by 1% isoflurane and placed in the prone position in a 34 °C water bath. During the imaging process, continuous anesthesia and oxygen were supplied through a mouse breathing mask. Imaging wavelengths selected conforming to the major turning points in NR-OH's and hemoglobin's absorption spectra included 680 nm, 685 nm, 690 nm, 695 nm, 700 nm, 710 nm, 720 nm, 730 nm, 740 nm, 750 nm, 760 nm, 770 nm, 780 nm, 800 nm (background), 825 nm and 850 nm. We recorded 5 frames at every imaging wavelength. The region, spanning through the liver and consisting of transverse slices with a step size of 0.1 mm, was selected by inspection of live MSOT images. After the MSOT images were generated, the z-stack was rendered as orthogonal-view three-dimensional images (guided ICA spectral unmixing was utilized to separate signals coming from the activated probe and those from the photo-absorbing tissue elements in the body (e.g. hemoglobin)).

Serum biochemistry assessment and tissue histological evaluation

Serum biochemistry indexes aminotransferase (ALT) was measured by Elisa kits. Mice were injected with NR-NO$_2$ solution (2.8 mg probe/kg body weight, in PBS containing 2% DMSO) through the tail vein 24 h prior to serum testing. For histological study, mice were treated with the probe 24 h in advance for the treatment groups and PBS for the control groups; organs (heart, liver, spleen, lung, and kidney) were excised and tissue-fixed for hematoxylin and eosin (H&E) staining.

Relative OA intensity

Relative OA intensity was used to indicate response of the probe to H_2S (NaHS was used as the H_2S donor) of varied concentrations for the optoacoustic method. It was calculated with the equation:

$$\text{Relative OA intensity} = [(OA_{695})_{NaHS} - (OA_{695})_{control}] / (OA_{695})_{control}$$

Results and Discussion

Design and synthesis of the probe NR-NO$_2$

The probe (NR-NO$_2$) was designed by adopting the strong electron-withdrawing group dinitrophenyl ether as the recognition moiety for H_2S and as the fluorescence quencher as well (Figure 1A). The structural characterizations (including ^1H NMR, ^{13}C NMR and ESI-MS) of probe and intermediates are shown in Figures S1-8. H_2S can break the dinitro-phenyl ether bond of NR-NO$_2$ [63, 64], thereby changing the chemical structure and leading to the formation of the activated form of the probe (NR-OH); and the structure of the product from the reaction of NR-NO$_2$ and NaHS (the reaction product was purified by silica gel column chromatography) was confirmed by ^1H NMR and HR-MS spectra (Figures S9-10). This response process strengthens the electron push-pull structure (donor-π-acceptor), and eventually results in the enhanced fluorescent emission for fluorescence imaging and red-shifted absorption band (Figure 1B) for optoacoustic imaging.

Spectral response of the probe NR-NO$_2$ toward H_2S

Spectral properties of the probe NR-NO$_2$ and the probe's response towards H_2S were investigated experimentally. First, absorption and fluorescence spectra of the probe in the presence of NaHS (H_2S donor) were measured (excitation wavelength at 680 nm). Figure 2A and 2B show the time-dependent changes in the absorption and fluorescence spectra. The probe was incubated with NaHS (60 µM) for 20 min, during which the spectra were measured every 2 min to record the detailed spectral responses. In the absence of H_2S, the probe exhibited a strong

absorption band centering around 560 nm and negligible fluorescence emission at 725 nm. Whereas in the presence of H2S, the absorption spectrum red-shifted and the absorption peaked around 695 nm and the fluorescence emission at 725 nm significantly enhanced as the incubation time prolonged. These prominent spectral changes were caused by the H2S-mediated structural transformation from NR-NO2 to NR-OH. Figure 2C shows the fluorescence spectra of NR-NO2 incubated with different concentrations of NaHS (0, 15, 30, 45 and 60 μM) for 20 min. From the spectra, we can see the response of the probe towards H2S is concentration-dependent. The absorbance at 695 nm and the fluorescent intensity at 725 nm of the probe incubated with different concentrations of NaHS as a function of time are shown in Figure S11A-B, and the data at each concentration for 20 min incubation were also recorded as shown in Figure S11C-D; and the results show a good NaHS concentration-dependent linear relationship. In addition, the limit of detection (LOD) towards NaHS was determined to be 40 nM (Figure S12A-B), which is comparable to the reported probes (Table S1). The fluorescence intensity reached plateau at higher substrate concentration (Figure S12C-D). Moreover, the probe is operable in the pH range of 6.5 – 7.8, as shown in Figure S13. To investigate the sensing selectivity, the probe NR-NO2 was treated with various potential biologically relevant species (e.g., representative anions, reducing agents, reactive

oxygen species and small-molecule thiols), followed by the fluorescence intensities measurement. As shown in Figure 2D, addition of the representative anions (Cl-, Br-, I-, NO3-, NO2-, CO3^2-, HCO3-, SO4^2-) at 1 mM, reducing agents (SO3^2-, S2O3^2-) at 100 μM, reactive oxygen species (ClO-) at 50 μM, and small-molecule thiols at the biologically relevant concentrations (1 mM for HCy, 1 mM for cysteine and 10 mM for GSH) couldn't induce marked fluorescence emission at 725 nm. In contrast, upon treatment with NaHS (60 μM) for 20 min, a remarkable 40-fold fluorescence enhancement was observed. The above results reveal that NR-NO2 has quite high selectivity towards H2S over various species tested including glutathione (GSH) and cysteine of the biologically-relevant concentrations, confirming that H2S-mediated thiolysis reaction of the dinitrophenyl ether is highly selective and other free thiols in the biological systems won't affect the probe's response toward H2S. The results are in agreement with literature reports in that the superior chemoselectivity for H2S is based on the striking difference in size and pKa values of H2S and other free thiols [65]. H2S has a smaller molecular size, which makes the chemical reaction with NR-NO2 easier. Additionally, the pKa value of H2S (around 6.9 [66]) is lower than that of typical cellular free thiols (around 8.5 [67]), all these contribute to the sensing selectivity under physiological conditions. Moreover, the extinction coefficient for NR-OH (the activated form of the probe) at 695 nm

Figure 1. (A) Synthetic route for the probe NR-NO2. (B) Absorption spectra of the probe NR-NO2 and its activated form NR-OH (10 μM). (C) A schematic representation of the probe's diagnosis of liver injury induced by metformin in mice model.

was calculated to be 2.2×10^4 M^{-1}cm^{-1}, which is sufficient for optoacoustic effect that converts the absorbed optical energy into heat, accompanied by generation of ultrasonic signal after thermal expansion. We next evaluated the probe's optoacoustic response toward H2S in phantom. The optoacoustic intensities (%) of NR-OH corresponding to different wavelengths measured by MSOT system were given in Figure S14. And relative optoacoustic intensity increases with increasing concentration of NaHS from Figure 2E. Moreover, the optoacoustic response specificity (selectivity) and anti-interference of NR-NO2 are shown in Figure 2F. And the experimental data indicate that the probe shows excellent optoacoustic response for H2S. These spectral results confirmed that NR-NO2 could be applied in imaging H2S by both fluorescent and optoacoustic methods.
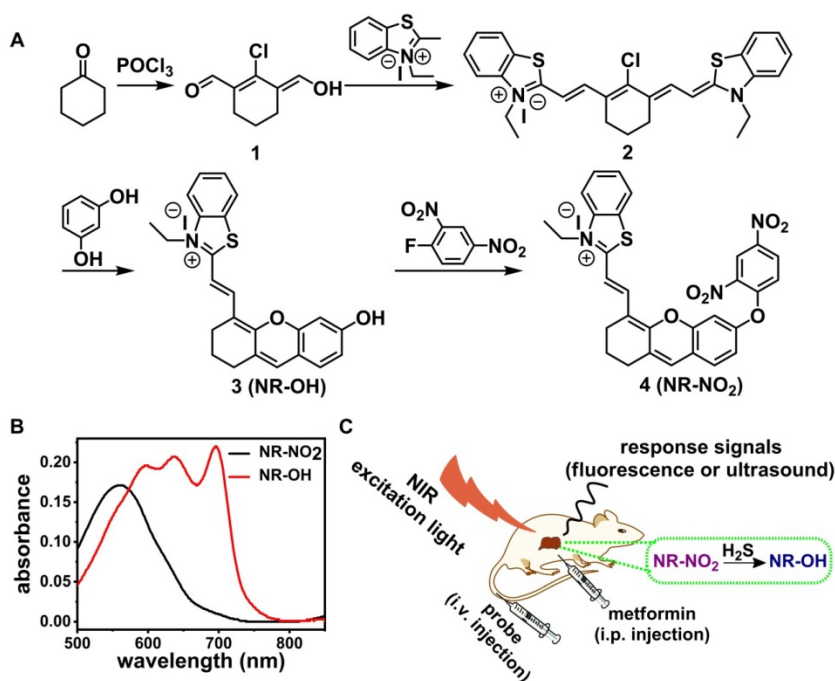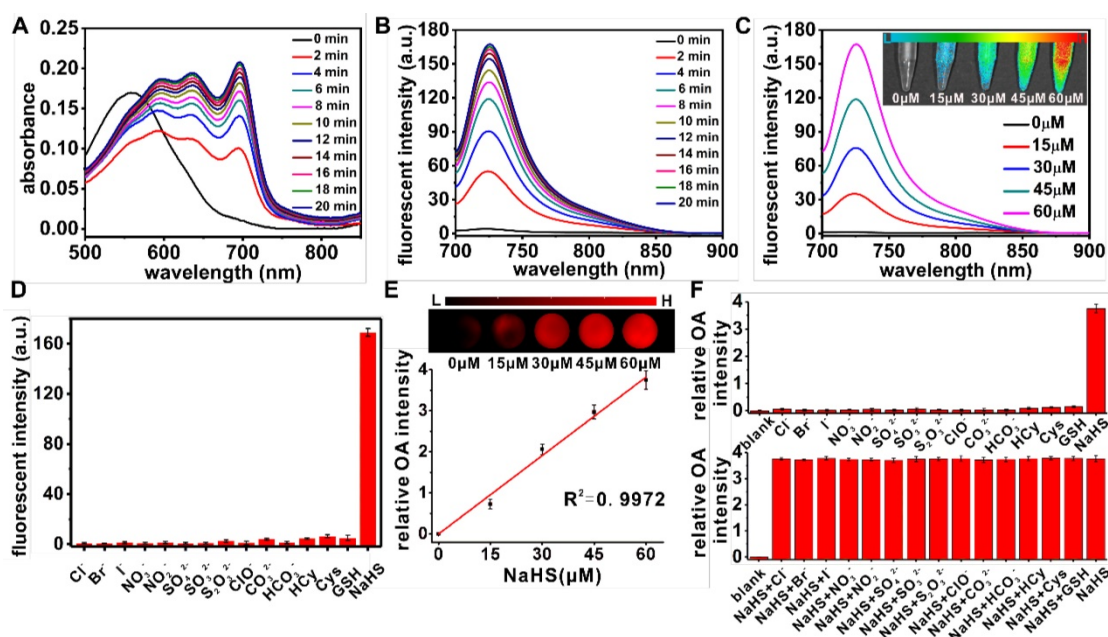
Figure 2. (A) Time-dependent absorption spectra of NR-NO₂ (10 μM) in the solution containing 60 μM NaHS. (B) Time-dependent fluorescence spectra of NR-NO₂ (10 μM) in the solution containing 60 μM NaHS with an excitation wavelength at 680 nm. (C) Fluorescence spectra of NR-NO₂ (10 μM) after 20 min incubation with different concentrations of NaHS (0, 15, 30, 45 and 60 μM). Inset shows representative fluorescent images of the probes in the presence of different concentrations of NaHS measured with Ami small animal imaging system (excitation filter of 675 nm and emission filter of 710 nm). (D) Fluorescent intensity at 725 nm of NR-NO₂ (10 μM) in the presence of different species (Cl⁻, Br⁻, I⁻, NO₃⁻, NO₂⁻, CO₃²⁻, HCO₃⁻, SO₄²⁻, HCy and Cysteine: 1 mM; SO₃²⁻, S₂O₃²⁻: 100 μM; ClO⁻: 50 μM; GSH: 10 mM; NaHS: 60 μM). (E) Optoacoustic response of NR-NO₂ (10 μM) towards different concentrations of NaHS (n=3). Inset shows the representative optoacoustic images of NR-NO₂ (10 μM) in phantom with different concentrations of NaHS. (F) Relative optoacoustic intensity of NR-NO₂ (10 μM) in the presence of different species respectively (upper row) and in the presence of both NaHS with a potential interference substance (lower row) (n=3) (concentrations of all species were consistent with D). Data were represented as mean ± SD.

Imaging intracellular H₂S in HCT-116 cells

Three cell lines were selected for the experiments, including L929 cells (mouse fibroblastic cells), HeLa cells (human cervical cancer cells), and HCT-116 cells (human colorectal carcinoma cells). H₂S is expressed in all these three cell lines, but its level is much higher in some cancer cells, especially in HCT-116 cells [68]. As shown in Figure S15, the probe NR-NO₂ shows low cytotoxicity to all these three cell lines. The viabilities of three cell lines can be maintained above 80%, even after 24 h of incubation with NR-NO₂ at the concentration of 50 μM. The low toxicity of the probe is advantageous for imaging endogenous H₂S in living cells. Then, we investigated cellular uptake of the probe NR- NO₂ and its H₂S-activated imaging in living cells. Figure S16 reveals that the cellular uptake and intracellular fluorescence emission of the probe were time-dependent by flow cytometry analysis. As the incubation time prolonged, the intracellular fluorescence emission became stronger, which means that more NR-NO₂ molecules were activated into NR-OH in the cells by endogenous H₂S. We further confirmed that the fluorescence response of the probe NR-NO₂ to endogenous H₂S by fluorescence microscopy imaging (Figure 3A-C). It is clear that, with the increase of the probe concentration or the prolongation of the culture

time, the fluorescence of the cells was enhanced, and the fluorescence of HCT-116 cells with the higher level of endogenous H₂S expression among the three cell lines was the strongest when incubated with 30 μM probe for 90 min, which was consistent with the results of flow cytometry analysis. Furthermore, to prove that the fluorescence signal was generated by endogenous H₂S in cells, we conducted relevant experiments using AOAA (as an inhibitor of CBS) to reduce H₂S level in cells. As shown in Figure 3D, fluorescence signal in HCT-116 pretreated with 200 μM AOAA for 30 min was negligible compared to that in the group without AOAA pretreatment.

Imaging endogenous and exogenous H₂S at tumor region or in peritoneal cavity in mouse models

To evaluate the applicability of the probe in H₂S detection and imaging *in vivo*, we investigated the probe's performance in HCT-116 tumor-bearing mice using both *in vivo* fluorescent and MSOT imaging. The tumor-bearing mice model was established by subcutaneous injection of HCT-116 cells at the back of nude mice. As shown in Figure 4A, the fluorescent signal in the tumor area was quite prominent only 10 min after the probe injection and gradually enhanced over time, indicating the feasibility of NR-NO₂ to

rapidly respond to endogenous H_2S in tumor for real-time imaging. Mean fluorescent intensities at region of interest (ROI) covering the tumor area were given in Figure S17. Then, we pretreated tumor-bearing mice with 100 nmol AOAA for 12 h, and then injected $NR-NO_2$ into tumor 30 min prior to *in vivo* imaging. As can be seen from Figure 4B, fluorescence signal was weak at 30 minutes after injection of $NR-NO_2$ into the back of healthy mice (the black circle drawn with a marker pen on the mouse back shows the injection position for control purpose), due to the low level of endogenous H_2S in this position. Moreover, AOAA treatment did significantly reduce intratumoral fluorescence signal, indicating that the expression of endogenous H_2S in the tumor was reduced and that the fluorescence signal was produced in response to H_2S. To verify the probe's imaging towards exogenous H_2S, we then injected NaHS into the tumor. As expected, a stronger fluorescence emission was observed after injection of NaHS (Figure 4C).
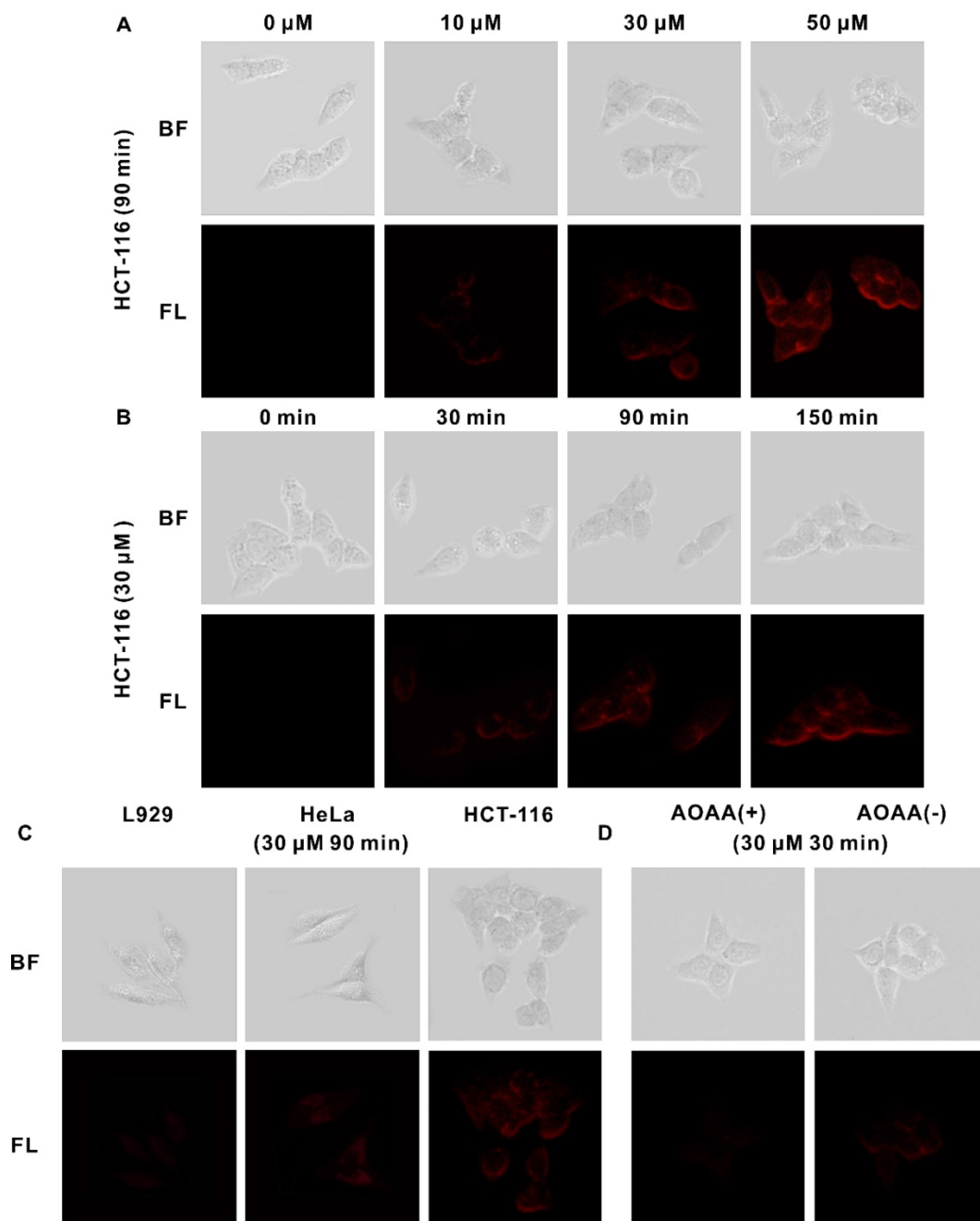

Figure 3. (A) Bright-field (top) and fluorescent (bottom) images of HCT-116 cells after incubation with different concentrations (0, 10, 30, 50 μM) of the probe for 90 min. (B) Bright-field (top) and fluorescent (bottom) images of HCT-116 cells after incubation with the probe (30 μM) for different period of time (0, 30, 90, 150 min). (C) Bright-field and fluorescent images of three cell lines after incubation with the probe (30 μM) for 90 min. (D) HCT-116 cells were incubated with the inhibitor AOAA (200 μM) for 30 min and then probe (30 μM) for 30 min (left), or with probe (30 μM) only for 30 min (right).
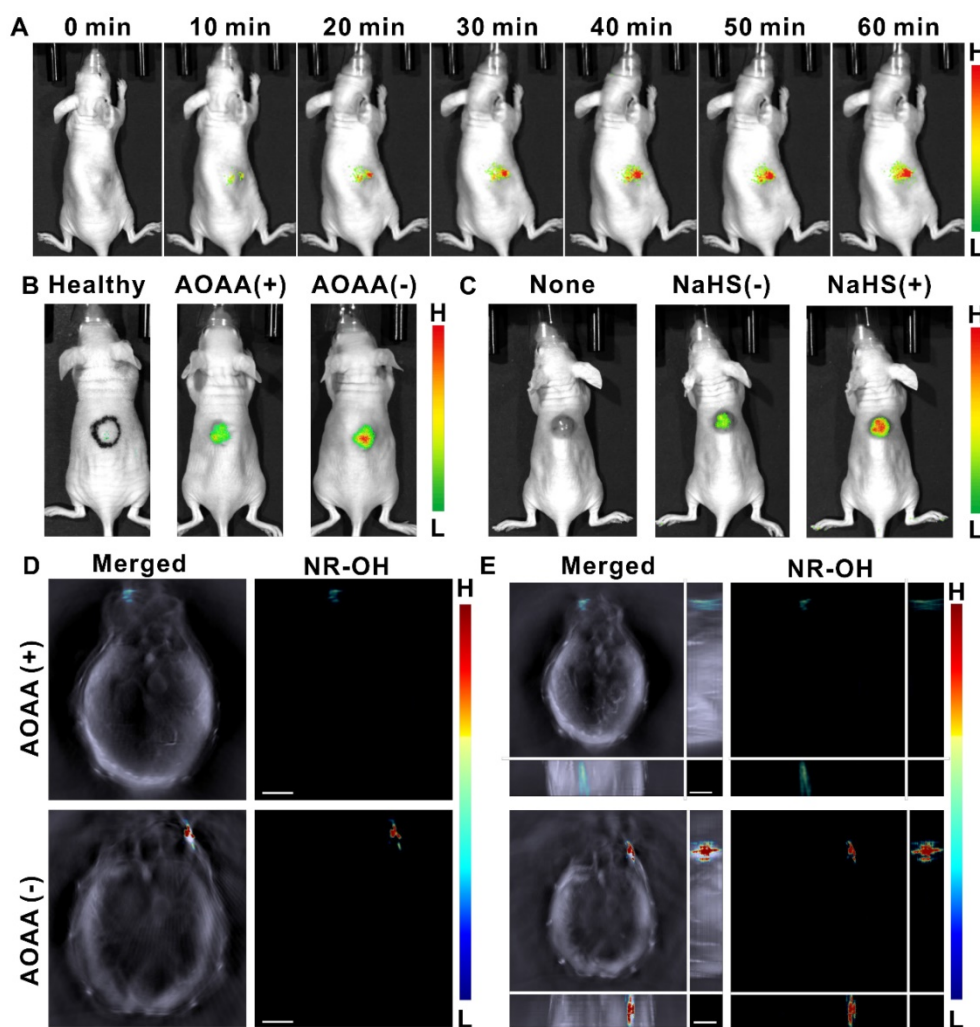
Figure 4. (A) Representative photographs for time-dependent response of the probe towards endogenous H_2S in mice tumor through intratumoral injection. (B) In vivo fluorescence imaging for healthy mice (left), AOAA-pretreated tumor-bearing mice (middle) and no-pretreatment tumor-bearing mice (right). (the black circle drawn with a marker pen on the mouse back shows the injection position for control purpose). (C) Representative photographs of tumor-bearing mice (left), in vivo fluorescence imaging towards endogenous (middle, 30 min after intratumoral injection of the probe) and exogenous (right, 30 min after intratumoral injection of the probe and 5 min after intratumoral injection of NaHS) H_2S in tumor-bearing mice. (D) Typical cross-sectional MSOT images (scale bar: 3 mm) of AOAA-pretreated tumor-bearing mice (upper row) or the tumor-bearing mice without AOAA pretreatment (lower row) at 30 min post intratumoral injection of the probe. (E) Typical orthogonal-view 3D MSOT images (scale bar: 3 mm) of AOAA-pretreated tumor-bearing mice (upper row) or tumor-bearing mice without AOAA pretreatment (lower row). Left: overlay of NR-OH (activated probe) signal with the grayscale single-wavelength (800 nm) background image; Right: NR-OH (activated probe) signal.

On the other hand, the real-time MSOT imaging provided further evidence that NR-NO$_2$ has excellent tumor imaging capability. It is worth mentioning that the orthogonal-view 3D MSOT images (z-stack orthogonal maximal intensity projection images) covering the whole tumor allows us to determine the relative position and the volume of solid tumors on the body of mice, more veritably and directly (Figure 4D-E). As expected, AOAA in tumors reduces the generation of endogenous H_2S, thereby attenuating H_2S-activated optoacoustic signal in tumors. In addition, we also evaluated the probe's capability to image H_2S in abdomina. As shown in Figure S18, through intratumoral injection, the probe can image H_2S of both endogenous and exogenous sources in the peritoneal cavity of mice. These results demonstrate that the probe NR-NO$_2$ can respond to both H_2S in tumor region and abdominal, and it can serve as a fluorescent/optoacoustic dual-mode molecular probe *in vivo*.

Diagnosing metformin-induced liver injury

Metformin overdose can cause increased H_2S level in mouse liver [17], which in turn induces liver injury. In this experiment, we established the metformin-induced liver injury mice model (metformin dose: 1 mg and 2 mg) to explore whether NR-NO$_2$ is capable of imaging the upregulation of hepatic H_2S and reflecting liver injury caused by metformin. First, by *in vivo* fluorescence imaging, we evaluated the metabolism of the probe NR-NO$_2$ injected through tail vein of the mice, and the results are shown in Figure S19. For the mice pretreated with 1 mg of metformin,

at one hour upon i.v. injection of the probe NR-NO$_2$, fluorescence in liver region emerged and reached the maximum at about 60 min post injection, then gradually faded due to the metabolism. This result is consistent with fluorescence imaging of the excised organs as displayed in Figure S20.

We then conducted optoacoustic imaging experiments. The mice were randomly assigned into three groups: the control group was injected (i. v.) with 200 µL of physiological saline at 10:00 a.m. every day for five consecutive days; and the two treatment groups were injected with 1 mg or 2 mg of metformin instead. On the fifth day, the mice were intravenously injected with the probe through tail vein and then subject to optoacoustic imaging. The MSOT system was used to monitor the severity of metformin-induced liver injury by imaging the elevated level of hepatic H$_2$S, and the results are presented in Figure 5. Figure 5A-C show the representative cross-sectional MSOT images from the mice at different time points in each group upon i.v. injection of the probe NR-NO$_2$. The upper row shows the overlay of NR-OH (activated probe) image with a single wavelength (800 nm) background image as the anatomical reference, while the lower row presents the MSOT signal from the activated probe NR-OH. For the control group treated with saline, only weak signal was detected in the liver (Figure 5A). In contrast, for the mice treated with metformin, the multispectrally resolved signal of NR-OH was significantly stronger and gradually increased over a period of 60 min (Figure 5B-C). Overdose of metformin caused upregulation of hepatic H$_2$S, and the probe molecules accumulated in the liver via metabolism were activated to produce optoacoustic signals. It can also be seen in the figure that, the mice exposed to 2 mg of metformin exhibited stronger MSOT signals. Moreover, the mean optoacoustic intensities in region of interest (ROI) over time were given in Figure 5D. By referring to a cryosection image of a mouse (Figure 5E), we can find that the signal of NR-OH is mainly located in the liver region, indicating an increase in the level of hepatic H$_2$S.

MSOT technique is capable of rendering multiple two-dimensional tomographic images as orthogonal-view 3D images (orthogonal maximal intensity projection images), which would aid in spatially positioning disease focus. In this study, we obtained orthogonal-view 3D images for the control mice as well as the mice groups treated with metformin, as shown in Figure 5G (at 30 min after i.v. injection of NR-NO$_2$). Upon treatment with metformin, hepatic H$_2$S levels were remarkably higher compared to that of the control group. Figure 5G also indicates that, the optoacoustic signal from the mouse treated with 2 mg of metformin was more evident compared to that treated with 1 mg of metformin, which verified the dose dependency of metformin to induce liver injury. Furthermore, to verify the biosafety and non-toxic nature of the probe, we performed some experiments, which include mice body weight tracking, H&E staining of liver sections, and serum liver function index measurement by using Elisa kits (Figure 5F and Figure S21-22). From Figure 5G, it can be seen that metformin administration leading to the increase of hepatic H$_2$S is dose dependent; and in combination with the results of serum tests as shown in Figure 5F, it is clear that the severity of liver injury is dependent on the extent of H$_2$S generation caused by the drug metformin. Figure S21 shows there was no abnormal change in mice weight within one week after i.v. injection of the probe, which indicated the low toxicity of the probe *in vivo*. Next, histological analysis of the main organs by using H&E staining (Figure S22) displayed that, there was no obvious difference between the control group and the mice group with i.v. injection of the probe, confirming the insignificant toxicity of the probe NR-NO$_2$ *in vivo*. While for the mice treated with metformin (Figure 5H), liver injury was evident for the mouse treated with 2 mg of metformin. Additionally, we measured the activities of serum alanine aminotransferase (ALT) by using Elisa kits and the results were given in Figure 5F. The data reveal that metformin overdose does cause liver injury to mice, and our probe has negligible effect on liver function. All the above experiments prove that, NR-NO$_2$ is of good biosafety and can be applied to detect the upregulation of hepatic H$_2$S and assess the severity of metformin-induced liver injury in mice model.

Conclusions

Taken all together, we have developed a novel molecular probe that specifically responds to H$_2$S, and it can be applied to imaging endogenous H$_2$S in HCT-116 tumor-bearing mice model. More importantly, it can also be used to monitor metformin-induced liver injury in mice model via detecting hepatic H$_2$S. With the aid of MSOT imaging method, the probe can be successfully used to distinguish and precisely position liver injury, and in the meantime visualize the volume of liver injury. Moreover, the probe NR-NO$_2$ exhibits quite good response specificity and sensitivity towards H$_2$S and good biosafety. The work herein could offer an optoacoustic probe for H$_2$S and an approach for designing chromophores for turn-on optoacoustic/fluorescent imaging, as well as provides helpful insights for devising an effective strategy for assessing the side effects of the drug by tracking its metabolism-related products.
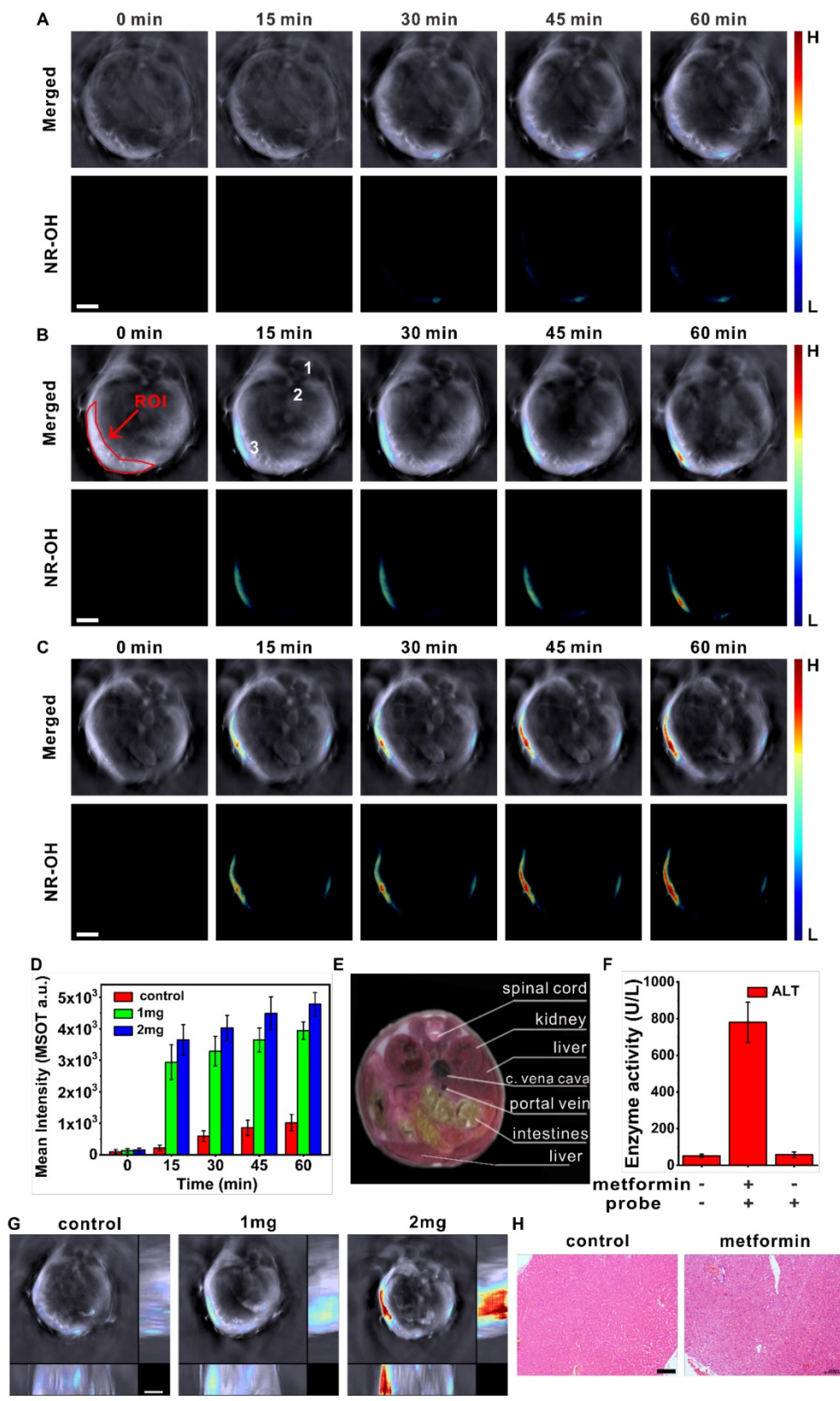
Figure 5. Typical cross-sectional MSOT images (scale bar: 3 mm) for a mouse treated with physiological saline (A), 1 mg (B) or 2 mg (C) of metformin at varied time post i.v. injection of the probe. Upper row: merged signals of NR-OH and the grayscale-wavelength (800 nm) background. Lower row: signal of NR-OH. Organ labeling: 1. spinal cord; 2. aorta; 3. liver. The mouse lay on its chest with a certain tilt as indicated by the position of spinal cord. (D) Mean optoacoustic intensities in liver area (ROI) for control mice and metformin-treated mice (n=6) at corresponding time post i.v. injection of the probe. (E) A cryosection image of a female mouse corresponding to the cross section shown in A-C. (F) Serum levels of ALT for the mice (n=6) with different treatment methods (+ means treatment, - means no treatment). (G) Orthogonal-view 3D MSOT images (scale bar: 3 mm) for the mice shown in A-C at 30 min post i.v. injection of the probe. (H) Representative H&E staining of liver sections from mice with different treatment methods: control mice (left) and 2 mg metformin-treated mice with probe injection at the fifth day. (Scale bar: 100 μm).

Supplementary Material

Supplementary figures and tables.

http://www.thno.org/v09p0077s1.pdf

Acknowledgment

Competing Interests

The authors have declared that no competing interest exists.

References

1. Joensuu H, Trent JC, Reichardt P. Practical management of tyrosine kinase inhibitor-associated side effects in GIST. Cancer Treat Rev. 2011; 37: 75-88.
2. Beakley BD, Kaye AM, Kaye AD. Tramadol, pharmacology, side Effects, and serotonin syndrome: a review. Pain Physician. 2015; 18: 395-400.
3. Illouz F, Braun D, Briet C, Schweizer U, Rodien P. Endocrine side-effects of anti-cancer drugs: thyroid effects of tyrosine kinase inhibitors. Eur J Endocrinol. 2014; 171: R91-9.
4. David S, Hamilton JP. Drug-induced liver injury. US Gastroenterol Hepatol Rev. 2010; 6: 73-80.
5. Zhang P, Jiang XF, Nie X, Huang Y, Zeng F, Xia X, et al. A two-photon fluorescent sensor revealing drug-induced liver injury via tracking gamma-glutamyltranspeptidase (GGT) level in vivo. Biomaterials. 2016; 80: 46-56.
6. Miller RA, Chu Q, Xie J, Foretz M, Viollet B, Birnbaum MJ. Biguanides suppress hepatic glucagon signalling by decreasing production of cyclic AMP. Nature. 2013; 494: 256-60.
7. Holman RR, Paul SK, Bethel MA, Matthews DR, Neil HA. 10-year follow-up of intensive glucose control in type 2 diabetes. N Engl J Med. 2008; 359: 1577-89.
8. Group UPDSU. Effect of intensive blood-glucose control with metformin on complications in overweight patients with type 2 diabetes (UKPDS 34). Lancet. 1998; 352: 854-65.
9. Gandini S, Puntoni M, Heckman-Stoddard BM, Dunn BK, Ford L, DeCensi A, et al. Metformin and cancer risk and mortality: a systematic review and meta-analysis taking into account biases and confounders. Cancer Prev Res (Phila). 2014; 7: 867-85.
10. Li L, Wang L, Li J, Fan Z, Yang L, Zhang Z, et al. Metformin-induced reduction of CD39 and CD73 blocks myeloid-derived suppressor cell activity in patients with ovarian cancer. Cancer Res. 2018; 78: 1779-91.
11. DeWaal D, Nogueira V, Terry AR, Patra KC, Jeon SM, Guzman G, et al. Hexokinase-2 depletion inhibits glycolysis and induces oxidative phosphorylation in hepatocellular carcinoma and sensitizes to metformin. Nat Commun. 2018; 9: 446.
12. Brynildsen JK, Lee BG, Perron IJ, Jin S, Kim SF, Blendy JA. Activation of AMPK by metformin improves withdrawal signs precipitated by nicotine withdrawal. Proc Natl Acad Sci U S A. 2018; 115: 4282-7.
13. Chen CB, Eurich DT, Majumdar SR, Johnson JA. Metformin and the risk of prostate cancer across racial/ethnic groups: a population-based cohort study. Prostate Cancer Prostatic Dis. 2017; 20: 122-6.
14. Deutsch M, Kountouras D, Dourakis SP. Case 1. Acute hepatitis due to metformin. Ann Intern Med. 2004; 140: 408-9.
15. Wilinski B, Wilinski J, Somogyi E, Piotrowska J, Opoka W. Metformin raises hydrogen sulfide tissue concentrations in various mouse organs. Pharmacol Rep. 2013; 65: 737-42.
16. Cone CJ, Bachyrycz AM, Murata GH. Hepatotoxicity associated with metformin therapy in treatment of type 2 diabetes mellitus with nonalcoholic fatty liver disease. Ann Pharmacother. 2010; 44: 1655-9.
17. Lin KD, Lin JD, Juang JH. Metformin-induced hemolysis with jaundice. N Engl J Med. 1998; 339: 1860-1.
18. Babich MM, Pike I, Shiffman ML. Metformin-induced acute hepatitis. Am J Med. 1998; 104: 490-2.
19. Kabil O, Banerjee R. Enzymology of H2S biogenesis, decay and signaling. Antioxid Redox Signal. 2014; 20: 770-82.
20. Yang G, Wu L, Jiang B, Yang W, Qi J, Cao K, et al. H2S as a physiologic vasorelaxant: hypertension in mice with deletion of cystathionine gamma-lyase. Science. 2008; 322: 587-90.
21. Abe K, Kimura H. The possible role of hydrogen sulfide as an endogenous neuromodulator. J Neurosci. 1996; 16: 1066-71.
22. Helmy N, Prip-Buus C, Vons C, Lenoir V, Abou-Hamdan A, Guedouari-Bounihi H, et al. Oxidation of hydrogen sulfide by human liver mitochondria. Nitric Oxide. 2014; 41: 105-12.
23. Norris EJ, Culberson CR, Narasimhan S, Clemens MG. The liver as a central regulator of hydrogen sulfide. Shock. 2011; 36: 242-50.
24. Hou X, Yu Q, Zeng F, Yu C, Wu S. Ratiometric fluorescence assay for gamma-glutamyltranspeptidase detection based on a single fluorophore via analyte-induced variation of substitution. Chem Commun (Camb). 2014; 50: 3417-20.
25. Wang S, Xi W, Cai F, Zhao X, Xu Z, Qian J, et al. Three-photon luminescence of gold nanorods and its applications for high contrast tissue and deep in vivo brain imaging. Theranostics. 2015; 5: 251-66.
26. Rong P, Yang K, Srivastan A, Kiesewetter DO, Yue X, Wang F, et al. Photosensitizer loaded nano-graphene for multimodality imaging guided tumor photodynamic therapy. Theranostics. 2014; 4: 229-39.
27. Wang H, Li X, Tse BW, Yang H, Thorling CA, Liu Y, et al. Indocyanine green-incorporating nanoparticles for cancer theranostics. Theranostics. 2018; 8: 1227-42.
28. Meng X, Yang Y, Zhou L, Zhang L, Lv Y, Li S, et al. Dual-responsive molecular probe for tumor targeted imaging and photodynamic therapy. Theranostics. 2017; 7: 1781-94.
29. Wu Y, Wang J, Zeng F, Huang S, Huang J, Xie H, et al. Pyrene derivative emitting red or near-infrared light with monomer/excimer conversion and its application to ratiometric detection of hypochlorite. ACS Appl Mater Interfaces. 2016; 8: 1511-9.
30. Yu C, Li X, Zeng F, Zheng F, Wu S. Carbon-dot-based ratiometric fluorescent sensor for detecting hydrogen sulfide in aqueous media and inside live cells. Chem Commun (Camb). 2013; 49: 403-5.
31. Li B, Liu P, Wu H, Xie X, Chen Z, Zeng F, et al. A bioorthogonal nanosystem for imaging and in vivo tumor inhibition. Biomaterials. 2017; 138: 57-68.
32. Li BW, Xie XW, Chen ZL, Zhan CY, Zeng F, Wu SZ. Tumor inhibition achieved by targeting and regulating multiple key elements in EGFR signaling pathway using a self-assembled nanoprodrug. Adv Funct Mater. 2018; 28: 1800692.
33. Hu Q, Yu C, Xia X, Zeng F, Wu S. A fluorescent probe for simultaneous discrimination of GSH and Cys/Hcy in human serum samples via distinctly-separated emissions with independent excitations. Biosens Bioelectron. 2016; 81: 341-8.
34. Qi Y, Huang Y, Li B, Zeng F, Wu S. Real-time monitoring of endogenous cysteine levels in vivo by near-infrared turn-on fluorescent probe with large Stokes shift, Anal. Chem. 2018; 90: 1014-20.
35. Chen Q, Liu X, Chen J, Zeng J, Cheng Z, Liu Z. A self-assembled albumin-based nanoprobe for in vivo ratiometric photoacoustic pH imaging. Adv Mater. 2015; 27: 6820-7.
36. Wu Y, Huang S, Wang J, Sun L, Zeng F, Wu S. Activatable probes for diagnosing and positioning liver injury and metastatic tumors by multispectral optoacoustic tomography. Nat Commun. 2018; 9: 3983.
37. Dean-Ben XL, Gottschalk S, Mc Larney B, Shoham S, Razansky D. Advanced optoacoustic methods for multiscale imaging of in vivo dynamics. Chem Soc Rev. 2017; 46: 2158-98.
38. Ntziachristos V, Razansky D. Molecular imaging by means of multispectral optoacoustic tomography (MSOT). Chem Rev. 2010; 110: 2783-94.
39. Taruttis A, Ntziachristos V. Advances in real-time multispectral optoacoustic imaging and its applications. Nat Photonics. 2015; 9: 219-27.
40. Lv J, Peng Y, Li S, Guo Z, Zhao Q, Zhang X, et al. Hemispherical photoacoustic imaging of myocardial infarction: in vivo detection and monitoring. Eur Radiol. 2018; 28: 2176-83.
41. Li W, Sun X, Wang Y, Niu G, Chen X, Qian Z, et al. In vivo quantitative photoacoustic microscopy of gold nanostar kinetics in mouse organs. Biomed Opt Express. 2014; 5: 2679-85.
42. Weber J, Beard PC, Bohndiek SE. Contrast agents for molecular photoacoustic imaging. Nat Methods. 2016; 13: 639.
43. Rosenthal A, Razansky D, Ntziachristos V. Quantitative optoacoustic signal extraction using sparse signal representation. IEEE Trans Med Imaging. 2009; 28: 1997-2006.
44. Razansky D, Buehler A, Ntziachristos V. Volumetric real-time multispectral optoacoustic tomography of biomarkers. Nat Protoc. 2011; 6: 1121-9.
45. Wang S, Lin J, Wang T, Chen X, Huang P. Recent advances in photoacoustic imaging for deep-tissue biomedical applications. Theranostics. 2016; 6: 2394-413.
46. Wang LV, Hu S. Photoacoustic tomography: in vivo imaging from organelles to organs. Science. 2012; 335: 1458-62.
47. Wilson KE, Bachawal SV, Abou-Elkacem L, Jensen K, Machtaler S, Tian L, et al. Spectroscopic photoacoustic molecular imaging of breast cancer using a B7-H3-targeted ICG contrast agent. Theranostics. 2017; 7: 1463-76.
48. Mallidi S, Watanabe K, Timerman D, Schoenfeld D, Hasan T. Prediction of tumor recurrence and therapy monitoring using ultrasound-guided photoacoustic imaging. Theranostics. 2015; 5: 289-301.
49. Rich LJ, Miller A, Singh AK, Seshadri M. Photoacoustic imaging as an early biomarker of radio therapeutic efficacy in head and neck cancer. Theranostics. 2018; 8: 2064-78.
50. Lu X, Zhao M, Chen P, Fan Q, Wang W, Huang W. Enhancing hydrophilicity of photoacoustic probes for effective ratiometric imaging of hydrogen peroxide. J Mater Chem B. 2018; 6: 4531-8.
51. Yin C, Zhu H, Xie C, Zhang L, Chen P, Fan Q, et al. Organic nanoprobe cocktails for multilocal and multicolor fluorescence imaging of reactive oxygen species. Adv Funct Mater. 2017; 27: 1700493.
52. Li H, Zhang P, Smaga LP, Hoffman RA, Chan J. Photoacoustic probes for ratiometric imaging of copper(II). J Am Chem Soc. 2015; 137: 15628-31.

53. Knox HJ, Hedhli J, Kim TW, Khalili K, Dobrucki LW, Chan J. A bioreducible N-oxide-based probe for photoacoustic imaging of hypoxia. Nat Commun. 2017; 8: 1794.
54. Xiao H, Wu C, Li P, Gao W, Zhang W, Zhang W, et al. Ratiometric photoacoustic imaging of endoplasmic reticulum polarity in injured liver tissues of diabetic mice. Chem Sci. 2017; 8: 7025-30.
55. Ntziachristos V. Going deeper than microscopy: the optical imaging frontier in biology. Nat Methods. 2010; 7: 603-14.
56. Tomaszewski MR, Gonzalez IQ, O'Connor JP, Abeyakoon O, Parker GJ, Williams KJ, et al. Oxygen enhanced optoacoustic tomography (OE-OT) reveals vascular dynamics in murine models of prostate cancer. Theranostics. 2017; 7: 2900-13.
57. Neuschmelting V, Kim K, Malekzadeh-Najafabadi J, Jebiwott S, Prakash J, Scherz A, et al. WST11 vascular targeted photodynamic therapy effect monitoring by multispectral optoacoustic tomography (MSOT) in mice. Theranostics. 2018; 8: 723-34.
58. Zhang K, Zhang J, Xi Z, Li LY, Gu X, Zhang QZ, et al. A new H2S-specific near-infrared fluorescence-enhanced probe that can visualize the H2S level in colorectal cancer cells in mice. Chem Sci. 2017; 8: 2776-81.
59. Lippert AR, New EJ, Chang CJ. Reaction-based fluorescent probes for selective imaging of hydrogen sulfide in living cells. J Am Chem Soc. 2011; 133: 10078-80.
60. Mao GJ, Wei TT, Wang XX, Huan SY, Lu DQ, Zhang J, et al. High-sensitivity naphthalene-based two-photon fluorescent probe suitable for direct bioimaging of H2S in living cells. Anal Chem. 2013; 85: 7875-81.
61. Ma T, Zheng J, Zhang T, Xing D. Ratiometric photoacoustic nanoprobes for monitoring and imaging of hydrogen sulfide in vivo. Nanoscale. 2018; 10: 13462-70.
62. Shi B, Gu X, Fei Q, Zhao C. Photoacoustic probes for real-time tracking of endogenous H2S in living mice. Chem Sci. 2017; 8: 2150-5.
63. Lin VS, Chen W, Xian M, Chang CJ. Chemical probes for molecular imaging and detection of hydrogen sulfide and reactive sulfur species in biological systems. Chem Soc Rev. 2015; 44: 4596-618.
64. Yu F, Han X, Chen L. Fluorescent probes for hydrogen sulfide detection and bioimaging. Chem Commun (Camb). 2014; 50: 12234-49.
65. Cao X, Lin W, Zheng K, He L. A near-infrared fluorescent turn-on probe for fluorescence imaging of hydrogen sulfide in living cells based on thiolysis of dinitrophenyl ether. Chem Commun (Camb). 2012; 48: 10529-31.
66. Mathai JC, Missner A, Kugler P, Saparov SM, Zeidel ML, Lee JK, et al. No facilitator required for membrane transport of hydrogen sulfide. Proc Natl Acad Sci U S A. 2009; 106: 16633-8.
67. Lutolf MP, Tirelli N, Cerritelli S, Cavalli L, Hubbell JA. Systematic modulation of Michael-type reactivity of thiols through the use of charged amino acids. Bioconjug Chem. 2001; 12: 1051-6.
68. Szabo C, Coletta C, Chao C, Modis K, Szczesny B, Papapetropoulos A, et al. Tumor-derived hydrogen sulfide, produced by cystathionine-beta-synthase, stimulates bioenergetics, cell proliferation, and angiogenesis in colon cancer. Proc Natl Acad Sci U S A. 2013; 110: 12474-9.